Acta Oceanol. Sin., 2025, Vol. 44, No. 3, P. 57–70
https://doi.org/10.1007/s13131-025-2463-7

Characteristics, interannual variation, and influence mechanisms of a double-halocline in the western Arctic Ocean during 2002 to 2022

Yu Zhang[2], Tao Li[1, 2*], Guoping Gao[3], Hongxin Zhang[4], Yubin Yao[2], Xingyuan Zhu[2], Yongjun Wang[2]

[1] Frontier Science Center for Deep Ocean Multispheres and Earth System (FDOMES) and Physical Oceanography Laboratory, Ocean University of China, Qingdao 266100, China

[2] College of Oceanic and Atmospheric Sciences, Ocean University of China, Qingdao 266100, China

[3] College of Oceanography and Ecological Science, Shanghai Ocean University, Shanghai 201306, China

[4] Beihai Bureau Support Center, Ministry of Natural Resources, Qingdao 266100, China

Received 8 December 2024; accepted 16 February 2025

© Chinese Society for Oceanography and Springer-Verlag GmbH Germany, part of Springer Nature 2025

Abstract

A halocline in the Arctic Ocean significantly slows the upward heat flux from deep warm water, thereby inhibiting the melting of surface sea ice. The western Arctic Ocean exhibits a double-halocline (DH) structure due to the complexity of the water mass. Using *in situ* measurements, we analyzed the vertical structural characteristics of DH and its interannual variation. The results indicated that the DH primarily occurs at the Northwind Ridge and the southern Canada Basin, extending westward to the Chukchi Abyssal Plain and northward to the northern boundary of the Canada Basin. From 2002 to 2022, there were changes in water masses that determined the structure of the DH. The significant increase in Pacific Water has resulted in 42% and 65% increases in freshwater and the heat content of the DH, respectively, along with a 14% reduction in stratification. Pacific Winter Water characterized by salinity of 33 has exhibited a gradually decreasing trend, suggesting that the lower halocline may be difficult to ventilate. The combined effects of Ekman pumping, mesoscale eddies, and positive buoyancy forcing (heat and freshwater input) from Pacific Water have altered the thickness and stratification of the DH. This study has enhanced our understanding of the evolution of vertical heat flux in the upper western Arctic Ocean.

Key words western Arctic Ocean, double-halocline, ocean stratification, buoyancy forcing

Citation Zhang Yu, Li Tao, Gao Guoping, Zhang Hongxin, Yao Yubin, Zhu Xingyuan, Wang Yongjun. 2025. Characteristics, interannual variation, and influence mechanisms of a double-halocline in the western Arctic Ocean during 2002 to 2022. Acta Oceanologica Sinica, 44(3): 57–70, doi: 10.1007/s13131-025-2463-7

1 Introduction

The Arctic Ocean, the smallest of the world's oceans, is connected to the Pacific Ocean through the Bering Strait and to the Atlantic Ocean via the Fram Strait, the Barents Sea opening, and the waterways among the Arctic Archipelago. The inflow into the Arctic Ocean is composed of high-salinity Atlantic Water (AW) and low-salinity Pacific Water. The Arctic Ocean is currently undergoing unprecedented warming (Zhao et al., 2015), with the upper 2 000 m warming at 2.3 times the global mean rate within this depth range averaged over the 21st century (Shu et al., 2022). This has resulted in a persistent decline in the extent of the summer sea ice, reaching a historic minimum of 3.34×10^6 km^2 in 2012 (Liu, 2022). The extent of sea ice in September 2020 was only half the average from 1979 to 2000 (Ye et al., 2024). In addition to solar radiation, the warm water inflow from the Atlantic constitutes a critical source of heat that influences the melting of sea ice (Shimada et al., 2006). After entering the Arctic Ocean, AW moves in a cyclonic manner along the continental slope as a boundary current. The substan-

Foundation item: The National Key Research and Development Program of China under contract No. 2023YFC2809101; the National Natural Science Foundation of China under contract No. 42276239.
*Corresponding author, E-mail: litaoocean@ouc.edu.cn

tial amount of heat the water carries affects the thermal balance of the Arctic Ocean, thereby contributing to the rapid retreat of sea ice (Zhang et al., 1998; Polyakov et al., 2010). As AW flows deeper, its heat progressively dissipates, establishing a pronounced halocline structure between the cold, fresh surface water and the warm, salty AW. This halocline is important for providing a density barrier trapping heat from the AW at depths away from the ice throughout the Arctic (Toole et al., 2010). If the halocline weakens or disappears, a substantial volume of meltwater will enter the North Atlantic, hindering deep water formation and consequently weakening the strength of Atlantic Meridional Overturning Circulation (Lin et al., 2023a). The strength of the halocline may serve as a novel indicator of climate change in the Arctic Ocean (Polyakov et al., 2018). The vertical structure of the halocline and its role in the variation of sea ice have become central topics in Arctic studies.

The Arctic Ocean is divided into the western Arctic Ocean and the eastern Arctic Ocean along 0° and 180° meridians. The eastern Arctic Ocean is characterized by a single vertical permanent halocline, called as cold halocline, whereas the western Arctic Ocean exhibits distinct halocline structure: a summer halocline, an upper halocline (UH), and a lower halocline (LH) in order from top to bottom. The summer halocline, commonly known as the seasonal halocline as it occurs exclusively in summer, is positioned between cold, fresh surface water (comprising sea ice meltwater and river freshwater) and warm, salty Pacific Summer Water (PSW). The UH is located between PSW and Pacific Winter Water (PWW). Pacific Water entering the Arctic Ocean via the Bering Strait sinks beneath the surface water and is subsequently transported laterally into the Beaufort Gyre (Timmermans et al., 2014, 2017). The sinking depth of Pacific Water varies between summer and winter. In winter, PWW becomes denser due to the formation of ice and brine rejection from coastal polynyas, ultimately sinking beneath the PSW (Weingartner et al., 1998; Shimada et al., 2005). The LH is positioned between the PWW and AW. AW from the Fram Strait and the Barents Sea opening is characterized by higher salinity than PWW, and thus, it will sink upon reaching the Beaufort Sea (Steele et al., 2004). Therefore, permanent double-halocline (DH), including UH and LH, formed by the advection mechanism that persists year-round (Aagaard et al., 1981; Shi et al., 2005).

The variation in the DH in the western Arctic Ocean is linked to processes at different spatial scales. Atmospheric forcing, the Arctic Oscillation anomaly, and increased glacial meltwater all contribute to changes in the salinity of surface seawater, subsequently resulting in variation in the halocline. In the southern Canada Basin, the clockwise-rotating, wind-driven Beaufort Gyre effectively traps a substantial amount of freshwater (McPhee et al., 2009). Darby and Bischof (2004) found that the Arctic Oscillation influenced the pathway of the transpolar drift, thereby affecting the drift trajectory of thick ice within the Beaufort Gyre and consequently influencing the freshwater content of the halocline. Climate warming has accelerated the melting of continental glaciers in Alaska, resulting in the freshening of Pacific Water (Chan et al., 2011). Based on long-term observational mooring data deployed at the Bering Strait, PWW is freshening at a rate of 0.03 per year in salinity, a rate that could influence the ventilation of the halocline. In addition, convective processes (Shimada et al., 2006; Woodgate et al., 2010), along with diffusion and double-diffusion phenomena (Bourgain and Gascard, 2011), contribute to alteration in the vertical structure of the halocline.

Significant changes have occurred in the DH due to the rapid decrease in sea ice and the increase in the heat content in the upper ocean. Further investigation is required to understand the mechanisms influencing the changes in the depth and thickness of the DH. Since the stratification of the halocline and the changes in the vertical heat flux through the DH have not been evaluated, we addressed these issues in the present study using comprehensive *in situ* hydrographic information and reanalysis data from 2002 to 2022. Section 2 describes the data and methods. Section 3 shows the variability of the DH and its corresponding influencing factors. The main conclusions are summarized in Section 4.

2 Data and methods

2.1 *In situ measurements*

The study area was divided into four regions based on topographical and circulation characteristics: the Chukchi Abyssal Plain (CAP), the Northwind Ridge (NwR), the northern Canada Basin (NCB), and the southern Canada Basin (SCB) (Fig. 1). The NwR and SCB are located at the center of the Beaufort Gyre, whereas the CAP and NCB are located at the edges of the gyre. We collected various *in situ* measurements of the western Arctic Ocean from 2002 to 2022 (Table 1). The principal scientific projects included the Chinese National Arctic Research Expedition (CHINARE), the Beaufort Gyre Exploration Project (BGEP), Ice Tether Profilers (ITP), the Unified Database for Arctic and Subarctic Hydrography (UDASH), and the World Ocean Database (WOD). Figure 1 depicts the distribution of the stations involving the DH structure from 2002 to 2022.

2.2 *Reanalysis data*

To quantify the interannual variability of the halocline, we used the GLORYS12 monthly global ocean reanalysis product provided by the Copernicus Marine Environment Monitoring Service. This product has a horizontal resolution of (1/12°) and comprises 50 vertical levels. Since the depth of the halocline is directly affected by Ekman pumping, we selected multi-source reanalysis data products to calculate the velocity of Ekman pumping and performed linear interpolation to obtain a monthly averaged dataset with a spatial resolution of 0.25° (latitude) ×

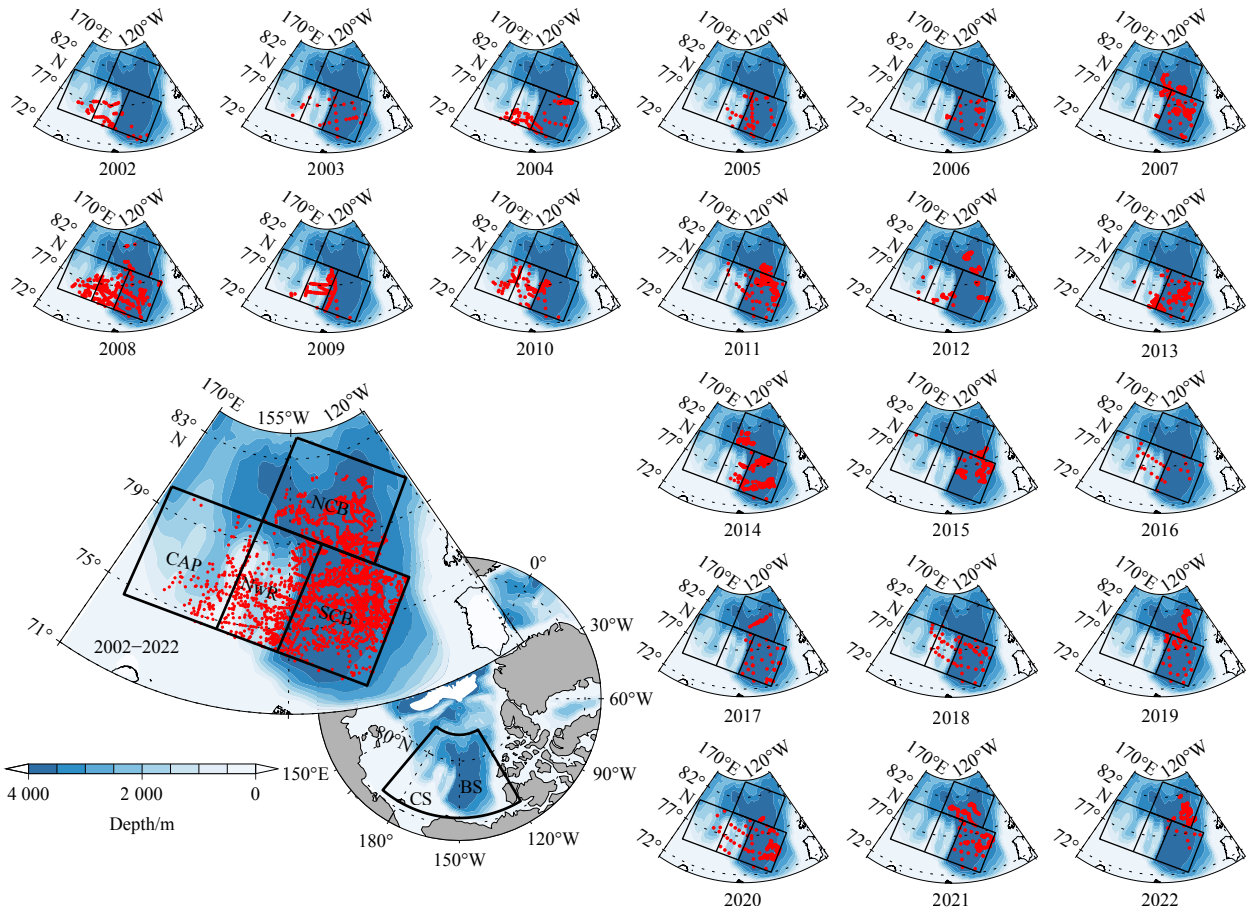


Fig. 1. Coverage of the composite historical *in situ* dataset. There are 5 166 stations showing the double-halocline (DH) structure from 2002 to 2022 with a wide distribution in 2008. CS: Chukchi Sea; BS: Beaufort Sea; CAP: Chukchi Abyssal Plain; NwR: Northwind Ridge; NCB: northern Canada Basin; SCB: southern Canada Basin.

Table 1. Summary of historical *in situ* hydrographic data

Projects	Year	Source
CHINARE	2003–2020	http://www.chinare.org.cn
BGEP	2003–2022	http://www.whoi.edu/beaufortgyre
ITP	2004–2022	http://www.whoi.edu/itp
UDASH	2002–2015	https://doi.pangaea.de/10.1594/PANGAEA.872931
WOD	2002–2022	http://www.ncei.noaa.gov/products/world-ocean-database

0.75° (longitude). The sea ice concentration and surface wind speed at 10 m were obtained from ERA5 released by the European Centre for Medium-Range Weather Forecasts (ECMWF); these data have a spatial resolution of 0.5° × 0.5° and a temporal resolution of 1 month. Sea ice drift data were obtained from Polar Pathfinder Daily 25 km EASE-Grid Sea Ice Motion Vectors, Version 4 released by the National Snow and Ice Data Center; the data have a spatial resolution of 25 km × 25 km and a temporal resolution of 1 month. Dynamic ocean topography (DOT) was obtained by a monthly averaged dataset produced by Armitage et al. (2020) that has a monthly (annual) average uncertainty of 1.1 cm (0.9 cm). The DOT features a spatial resolution of 0.25° (latitude) × 0.75° (longitude) and covers a range from 70.0°N to 81.5°N. The temporal resolution is 1 month, and the temporal range extends from 2003 to 2020.

2.3 *Methods for determining DH boundaries*

Although isohalines and isopycnals have commonly been used to delineate the boundaries of the halocline (Rudels et al., 1996; Korhonen et al., 2013; Polyakov et al., 2020), the freshening of Pacific Water (Woodgate and Peralta-Ferriz, 2021) introduces errors using these methods on a time scale of decades. According to Bertosio et al. (2022), the boundaries of the UH are determined based on the core location of the water masses. The *in situ* observations suggest that the UH can form when the temperature difference between the PSW and PWW exceeds 0.3℃. Therefore, the top boundary of the UH is determined by the core of the PSW (Fig. 2), specifically at the depth of temperature maximum within the salinity of 29–33 and deeper than 40 m. The PSW core is primarily composed of Alaska Coastal Water (ACW, 29–32.2 in

salinity), with minor proportions of summer Bering Sea Water (BSW, 29.2–33 in salinity) (Steele et al., 2004). ACW is regarded as the PSW core when both water masses are present, whereas BSW becomes the PSW core only due to a lack of ACW. The bottom boundary of the UH, which also serves as the top of the LH, is defined by the PWW core, identifying the temperature minimum within a salinity of 32.7–33.3.

The base of the LH was determined using the density gradient ratio (R) proposed by Bourgain and Gascard (2011). This ratio is defined as a function of both the temperature and salinity gradients:

$$R = \alpha \Delta T / (\beta \Delta S), \tag{1}$$

where α represents the thermal expansion coefficient; β denotes the saline contraction coefficient; ΔT and ΔS indicate changes in temperature and salinity in 1 m intervals. A smaller R value indicates a stronger salinity gradient but a weaker temperature gradient, a key characteristic of the structure of a halocline. The observational data indicated that $R = 0.05$ yielded the best fit for the LH base.

2.4 *Quantification of DH characteristics*

The accumulation of freshwater content (FWC) and heat content (HC) within the halocline influences the thermodynamic and dynamic processes in the upper ocean, thereby affecting the large-scale thermohaline circulation. Freshwater content is defined as

$$\mathrm{FWC} = \int_{z_1}^{z_2} (S_{\mathrm{ref}} - S)/S \, \mathrm{d}z, \tag{2}$$

where z_1 represents the depth of the halocline bottom; z_2 denotes the depth of the halocline top; S_{ref} is the reference salinity of 34.8.

Heat content is defined as

$$\mathrm{HC} = \int_{z_1}^{z_2} \rho C_{\mathrm{p}} (\theta - \theta_{\mathrm{f}}) \mathrm{d}z, \tag{3}$$

where ρ represents the density of seawater; θ and θ_{f} are the potential temperature and freezing point, respectively. C_{p} is the specific heat capacity of seawater, a function of the salinity and potential temperature.

Given that the DH in the western Arctic Ocean comprises multiple water masses, the Brunt-Väisälä Frequency (N^2), also known as the buoyancy frequency, was calculated to evaluate the stratification of the water column:

$$N^2 = -g \partial \rho / \rho \partial z, \tag{4}$$

$$N^2_{\mathrm{mean}} = \int_{z_1}^{z_2} N^2 \mathrm{d}z / \Delta h, \tag{5}$$

where g is the acceleration of gravity; ρ indicates the den-

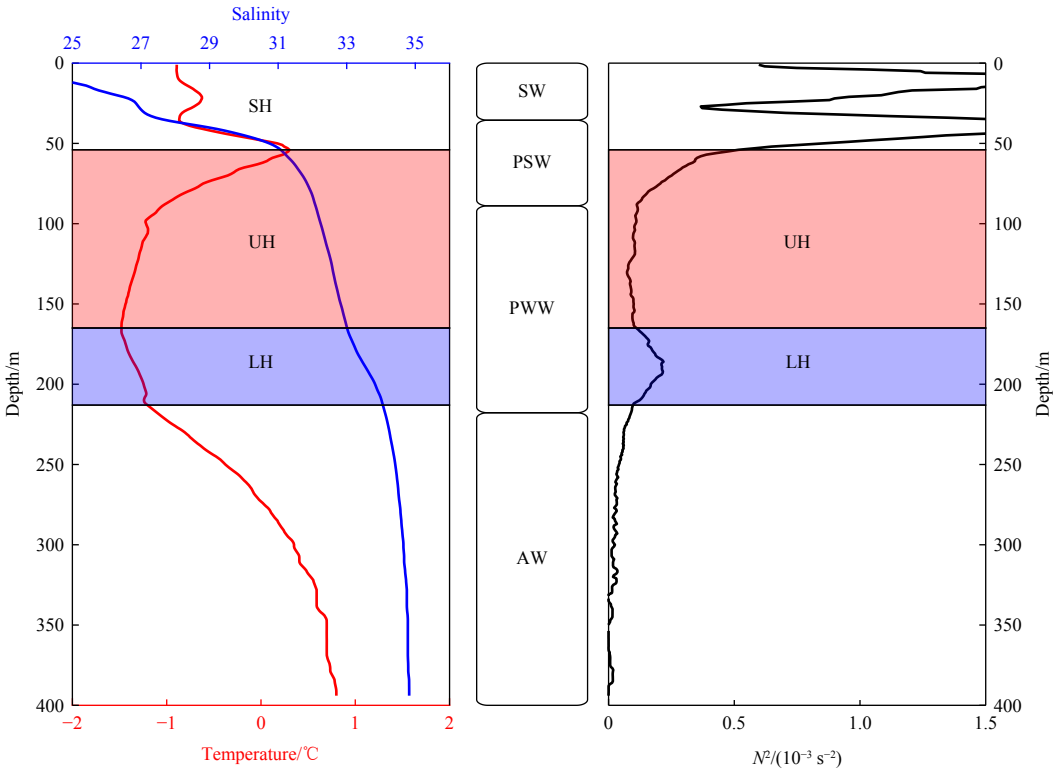


Fig. 2. Typical profiles of salinity (shown in blue; the top x-axis of the left panel), temperature (shown in red; the bottom x-axis of the left panel), and buoyancy frequency (shown in black; right panel) for a single cast at a station (76.0°N, 140.0°W) on August 21, 2007. The DH is delimited by horizontally shaded segments. Water masses are schematically plotted in the middle panel. SW: Surface Water; PSW: Pacific Summer Water; PWW: Pacific Winter Water; AW: Atlantic Water; SH: Summer Halocline; UH: Upper Halocline; LH: Lower Halocline.

sity of seawater; Δh is the difference between z_1 and z_2.

Vertical heat flux (F_h) caused by diapycnal mixing is defined as

$$F_h = \rho C_p k(\theta_1 - \theta_2)/(z_1 - z_2), \tag{6}$$

where ρ represents the density of seawater; θ_1 is the potential temperature at the halocline bottom; θ_2 is the potential temperature at the halocline top. k is the diapycnal diffusivity, here we assume a constant $k = 2 \times 10^{-6}$ m^2/s (Lique et al., 2014).

Ekman pumping can affect the boundaries of the DH via vertical movement of the water parcels; this is numerically equivalent to the stress curl acting on the ocean surface (Hibler III, 1979; Hibler III and Bryan, 1987). In open water, the ocean surface stress $\vec{\tau}_{ao}$ is a function of the surface wind speed $\vec{U}_s$. According to Zhong et al. (2018), the ocean surface stress $\vec{\tau}_{io}$ in regions covered by sea ice is a function of the difference between ice motion $\vec{U}_{ice}$ and geostrophic flow $\vec{U}_{oce}$ below the Ekman layer. We neglected the vertical variation in Ekman pumping (Kenigson et al., 2021), and the resulting formulas were as follows:

$$W_e = \nabla \times \vec{\tau}_{total}/(f\rho_w), \tag{7}$$

$$\vec{\tau}_{total} = \alpha\vec{\tau}_{io} + (1-\alpha)\vec{\tau}_{ao}, \tag{8}$$

$$\vec{\tau}_{ao} = \rho_a C_d \left|\vec{U}_s\right| \vec{U}_s, \tag{9}$$

$$\vec{\tau}_{io} = \rho_w C_{iw} \left|\vec{U}_{ice} - \vec{U}_{oce}\right| \left[(\vec{U}_{ice} - \vec{U}_{oce})\cos\theta + \vec{k} \times (\vec{U}_{ice} - \vec{U}_{oce})\sin\theta\right], \tag{10}$$

where α is the ice concentration; the air density ρ_a = 1.25 kg/m^3; the atmospheric drag coefficient C_d = 1.25 × 10^{-3}; the seawater density ρ_w = 1 023 kg/m^3; and the ice-ocean drag coefficient C_{iw} = 5.5 × 10^{-3}. Since $\vec{U}_{oce}$ is positioned beneath $\vec{U}_{ice}$, a reversal of the angle (i.e., 25°) is necessary to define the relationship between the two (Zhong et al., 2018).

Ekman pumping gives rise to a baroclinically unstable tilt of isopycnals, generating mesoscale eddies that reduce their slope via along-isopycnal fluxes. Consequently, the total transport in an isopycnal layer is known as the residual mean defined by $\Psi^{res} = \overline{\Psi} + \Psi^*$. The residual circulation Ψ^{res} through a layer has a component eddy-induced circulation Ψ^* in addition to the Eulerian mean $\overline{\Psi}$ because there can be correlations between the lateral flow and the thickness of the layer, leading to a significant bolus transport (Timmermans and Marshall, 2020). Meneghello et al. (2017) showed that if the lateral transport of Pacific Water is ignored, the residual circulation within the steady Beaufort Gyre is small enough to maintain an equilibrium between $\overline{\Psi}$ and Ψ^*. The Eulerian mean circulation can be expressed in terms of Ekman pumping as $\overline{\Psi} = \overline{\tau}/(\rho_0 f)$. The eddy-induced circulation can be represented by the horizontal buoyancy flux as $\Psi^* = \overline{v'b'}/(\partial\overline{b}/\partial z)$. This leads to $\overline{v'b'} = -K_D(\partial\overline{b}/\partial r)$, resulting in $\Psi^* = K_D I$. Here, I denotes the slope of the halocline, and K_D represents the eddy diffusion when the residual circulation is zero. Ultimately, we could derive a formula

$$I = -\overline{\tau}/(K_D\rho_0 f), \tag{11}$$

which indicates that the slope of the halocline is jointly determined by surface stress and the eddy buoyancy diffusivity.

3 Results and discussion

3.1 *Spatial distribution of the DH*

Figure 1 shows that the spatial coverage of the DH over the western Arctic Ocean is primarily centered around the Northwind Ridge and the southern Canada Basin. The UH is composed of PSW and PWW, whereas the LH is composed of PWW and may also include a minor proportion of AW in certain areas. There is a strong correspondence between the DH and N^2, with the UH demonstrating low N^2 values and the LH exhibiting high N^2 values (Fig. 2). This phenomenon can be attributed to the differences in temperature and salinity between the PSW and PWW. During winter, the PWW becomes denser due to the formation of ice and brine rejection in polynyas, resulting in the formation of the LH. The vertical density gradient of the PWW is more pronounced than that of the PSW, resulting in the water column being less susceptible to displacement.

Given that hydrographic stations in 2008 were distributed widely in the West Arctic Ocean (Fig. 1), we chose this year to examine the differences in the DH across the four regions. The results showed the DH occurred at a depth of 41–257 m in 2008 (Figs 3a–c), with the UH exhibiting a thickness of (97 ± 36) m and the LH being approximately (55 ± 21) m thick. From CAP and NCB to NwR and SCB, the DH deepened from 41–177 m to 98–257 m. These spatial distributions reflected the fundamental characteristics of the Beaufort Gyre. In 2008, the center of the Beaufort Gyre was situated in NwR and SCB, where Ekman transport caused a substantial accumulation of freshwater, leading to increased sea surface height and downwelling (Shimada et al., 2005). Consequently, the halocline was deeper in NwR and SCB than in CAP and NCB. Furthermore, the strength of downwelling was influenced by surface wind, the concentration of sea ice, and geostrophic flow. In 2008, the total stress input led to an Ekman pumping velocity twice the climatological average (Figs 3h and i), resulting in a deeper DH.

The thickness of the DH did not have a consistent spatial distribution with depth. In 2008, both UH and LH reached their maximum thickness at NwR, gradually decreasing toward the surrounding regions (Fig. 4). The dis-

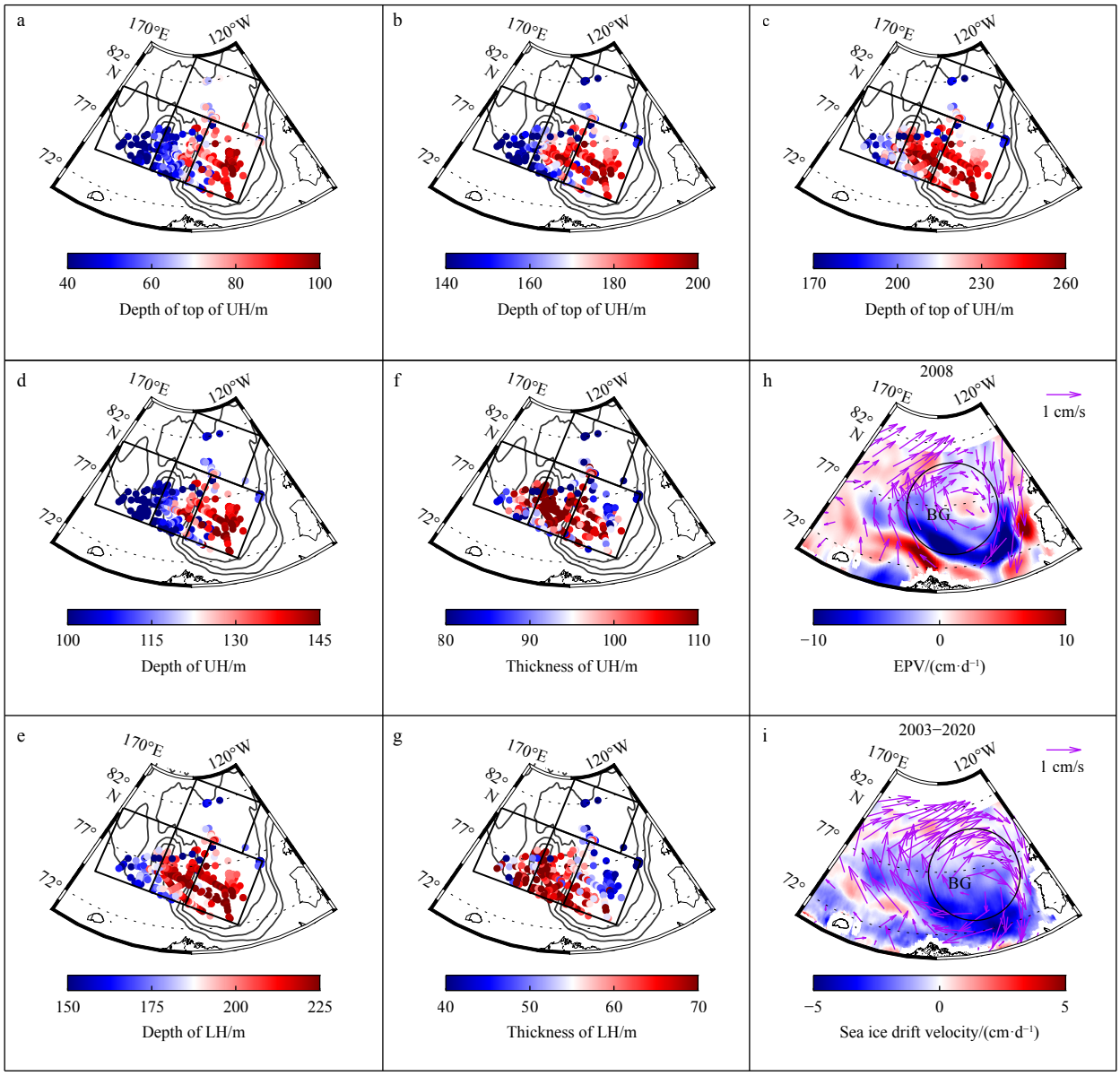


Fig. 3. Depths of the boundaries of the DH (a–c), the depth (d and e) and thicknesses (f and g) of the upper halocline (UH) and lower halocline (LH) in 2008 (*in situ* data, colored dots), the mean Ekman pumping velocity (EPV, colored shading, a negative EPV value indicates a downward flow) in 2008 (h), and sea ice drift velocity (purple vectors) during 2003–2020 (i).

crepancy between the locations of maximum halocline thickness and maximum Ekman pumping velocity indicated that the central position of the Beaufort Gyre was not the main factor influencing halocline thickness. Furthermore, a BSW-type DH structure was present in NCB, leading to a thicker and deeper UH.

3.2 *Interannual variation of the DH*

From 2002 to 2022, the regionally averaged depth of the UH showed a generally increasing trend, but there was significant phase variation (Figs 5a and b). Between 2002 and 2008, the UH and LH deepened rapidly by (36 ± 11) m, while both exhibited only minor fluctuations in the following 14 a until 2022. During the same period, the thickness of the UH across the four regions increased by (31 ± 14) m, exhibiting a trend similar to the UH depth (Figs 5c and d). The changes in the thickness of the LH were particularly notable, being characterized by a sharp decrease from 2002 to 2007, a rapid increase from 2007 to 2010, and a gradual decrease from 2010 to 2022. Between 2002 and 2010, the LH thickness exhibited a reverse pattern, whereas the UH thickness consistently demonstrated a trend of stable increase. This indicates that the UH and LH thickness are not in a compensatory relationship, thereby ruling out the possibility of the LH water crossing into the UH.

In the four regions, the freshwater content of the UH was nearly three times that of the LH (Fig. 5e). According to Eq. (2), two factors jointly influence the freshwater content within the DH: seawater salinity relative to

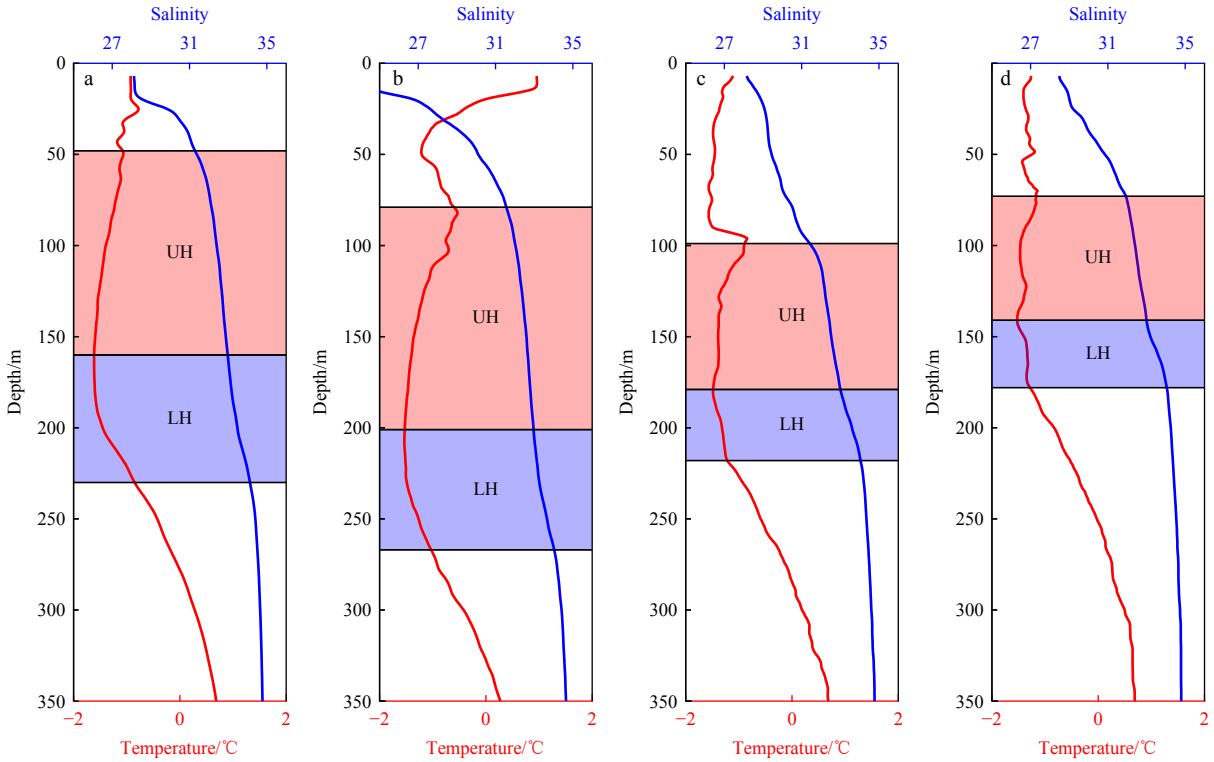


Fig. 4. Example profiles of salinity (blue; top *x*-axis) and temperature (red; bottom *x*-axis) in CAP (a), NwR (b), NCB (c), and SCB (d).

34.8 and the thickness of the halocline. However, the latter was the primary factor, as indicated by the Pearson correlation of 0.91. Lin et al. (2023a) pointed out that from 2003 to 2019, the total freshwater content in the seasonal and permanent halocline increased from 14.6 m to 20.0 m, with an increase of 37%. We found that the average freshwater content of the UH increased from (6.7 ± 2.4) m to (9.5 ± 3.8) m from 2002 to 2022 due to an increase in thickness. This 42% increase reflects the significant freshening of Pacific Water. Although the freshwater content of the LH experienced fluctuations between 2002 and 2010, the level gradually recovered to (2.0 ± 0.2) m in the subsequent period (Fig. 5f). The heat content of the UH increased from (2.1 ± 0.3) × 10^8 J/m^2 in 2002 to approximately (4.0 ± 1.4) × 10^8 J/m^2 in 2022 (Fig. 5g). This nearly 100% increase indicated significant warming of Pacific Water. Timmermans et al. (2018) attributed this warming effect to the melting of sea ice in the Chukchi Sea and the increase in solar radiation entering the surface ocean in summer. The heat content of the LH did not change notably during this period (Fig. 5h).

3.3 *Mechanisms of influencing depth and thickness of the DH*

3.3.1 *Equilibrium between Ekman pumping and mesoscale eddy activity*

We could estimate the slope of the halocline using surface stress and the eddy buoyancy diffusivity according to Eq. (11). However, K_D cannot be measured directly. Zhong et al. (2019a) calculated the actual eddy diffusivity K_λ in the Beaufort Gyre from 80 m to 400 m using climatological data, and they chose a constant value of 500 m^2/s as the typical eddy diffusivity, assuming that there is no additional lateral advection or injection of PWW. Thus, $\Delta h = \bar{\tau}\Delta L/(K_D\rho_0 f) \approx 27$ m, where $\bar{\tau} = 5 \times 10^{-3}$ N/m^2, $f = 1.5 \times 10^{-4}$ S^{-1}, $K_D = 500$ m^2/s, and $\Delta L = 400$ km (the radius of the Beaufort Gyre). The results were generally consistent with observational data. The difference in the depth of the LH between the central region (NwR and SCB) and the edge region (CAP and NCB) of Beaufort Gyre is (32 ± 16) m (Fig. 6). Therefore, on a climatological timescale, the balance between Ekman pumping and mesoscale eddy activity governs the intensity of depression of the halocline across different regions.

Analysis of the interannual variation of the halocline identified a strong correlation between the Ekman pumping velocity and the upper boundary depth of the UH (Fig. 6). In NwR, NCB, and SCB, the Pearson correlations exceeded 0.60, with SCB reaching as high as 0.81. These strong correlations indicate that Ekman pumping predominates for the upper boundary depth of the UH. Furthermore, the LH is sensitive to upper ocean pressure due to its relative thinness. From 2002 to 2007, the sea ice conditions in the western Arctic transitioned from multi-year ice to first-year ice, accompanied by a strengthening of surface winds. This change increased the total stress curl input into the ocean and enhanced Ekman pumping (Zhong et al., 2019b), leading to a decrease in the thickness of the LH (Figs 5d and 6). After 2007, both sea ice and wind speed gradually returned to normal climatologi-

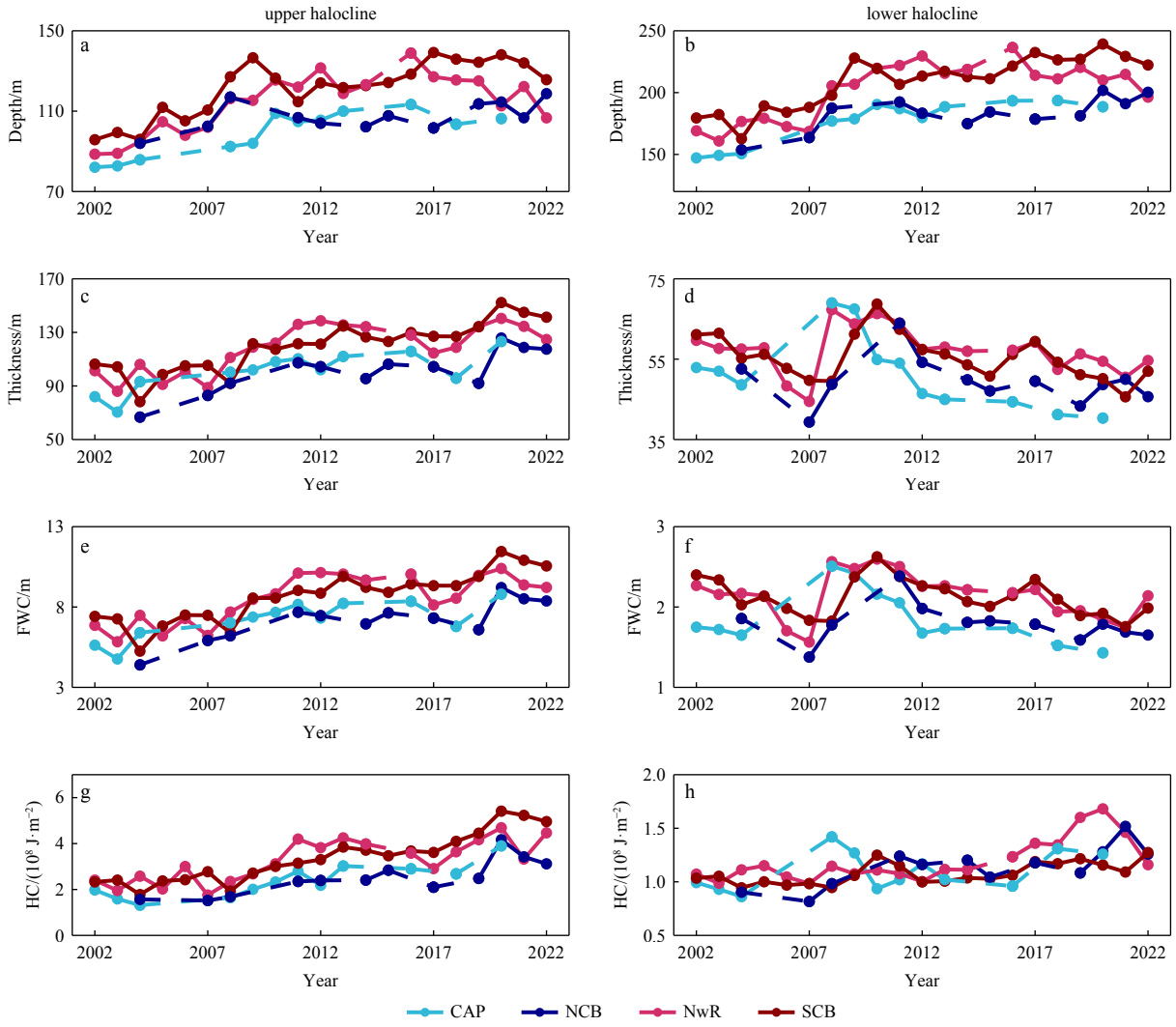


Fig. 5. Time series of regional averages of depth (a and b), thickness (c and d), freshwater content (FWC) (e and f), and heat content (HC) (g and h) of the upper and lower haloclines during the period 2002–2022.

cal levels, and the thickness of the LH also recovered to (50 ± 7) m.

From 2002 to 2022, there was a stable deepening trend of the LH in the four regions that cannot be explained by Ekman pumping (Fig. 6). The average deepening rate of the upper boundary was (3.1 ± 0.3) m/a; the lower boundary was (2.7 ± 0.5) m/a. We think this phenomenon may be related to the positive buoyancy forcing of Pacific Water.

3.3.2 *Buoyancy forcing from Pacific Water*

The newly ventilated Pacific Water that determines the structure of DH becomes warmed by solar radiation and freshened by melting sea ice. We selected a long-span station (78.0°N, 140.0°W) for the period 2004–2018 to illustrate the impacts of positive buoyancy forcing (Fig. 7). The PWW core deepened from (132 ± 9) m to (173 ± 6) m. In the long term, the newly ventilated Pacific Winter Water (NPWW) became fresher and warmer, resulting in a shallower neutral buoyancy depth. The old Pacific Winter Water (OPWW) demonstrating an oxygen minimum (Fig. 7d) sank due to the intrusion of the NPWW. Also, newly ventilated Pacific Summer Water (NPSW) occupied the position originally held by old Pacific Summer Water (OPSW), leading to the sinking of OPSW.

In fact, not only is the Pacific Water at this station became fresher and warmer, but the entire Western Arctic Ocean was undergoing this change. Based on the trends of the DH thickness, we selected 2003–2007 and 2016–2020 for comparative analysis. The *in situ* data and GLORYS12 were utilized to calculate the thickness of the UH and LH, with results shown in Table 2. In the four areas, the halocline thickness error between the two data sets is less than 11%. Therefore, we thought GLORYS12 could reflect changes in Pacific Water volume, providing a basis for a more detailed assessment.

For each grid in GLORYS12, the volumes of water masses within 40–400 m were calculated with a resolution of ΔS_r = 0.1, and the volumes corresponding to the same salinity were aggregated. We can see an increase in the volume of low-salinity water, which is the manifestation of freshening in the PSW (Fig. 8). The volume series of water masses for the two periods was then differenced.

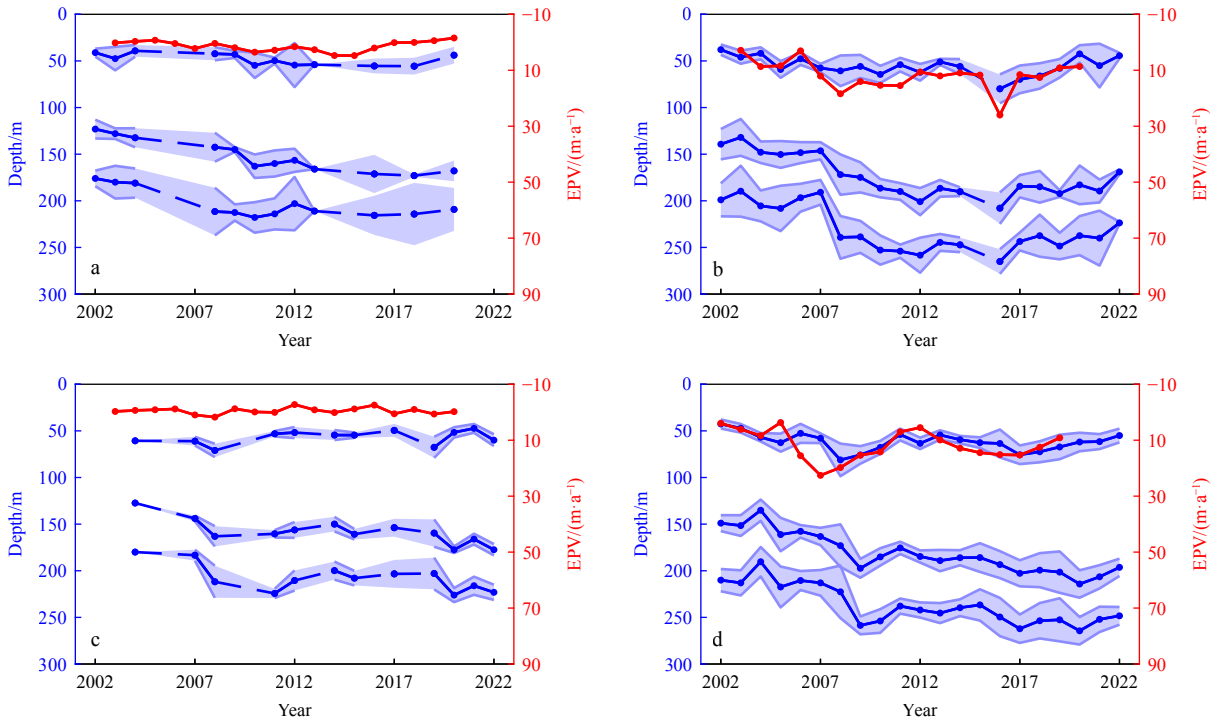


Fig. 6. Interannual variation of the depth of boundaries (blue curve) versus Ekman pumping velocity (EPV) (red curve) in CAP (a), NwR (b), NCB (c), and SCB (d). The blue shadows show standard errors at a 95% confidence level.

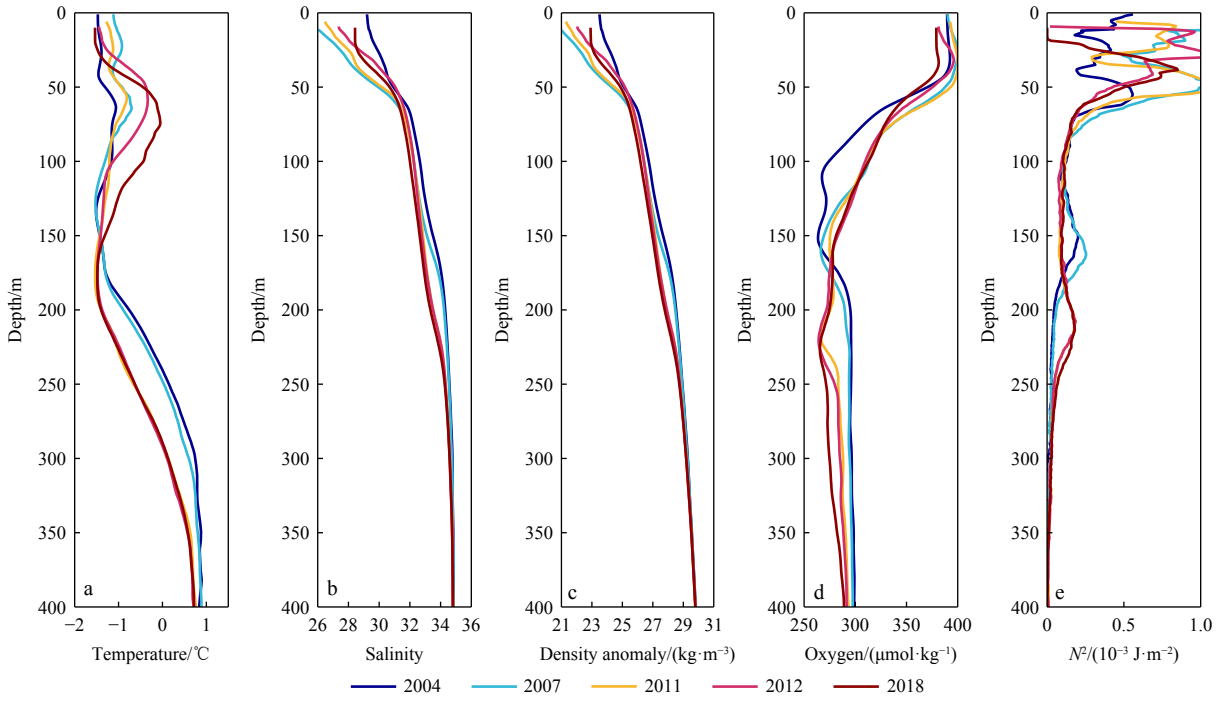


Fig. 7. Profiles of temperature (a), salinity (b), density anomaly (c), oxygen concentration (d), and buoyancy frequency (e) at the station (78.0°N, 140.0°W) during the period 2004–2018.

The results showed that the core salinities of OPSW and OPWW we calculated from *in situ* data (red and blue dots in Fig. 9) corresponded precisely to the minimum volume differences in CAP, NwR, and SCB and that the core salinity of NPSW corresponded to the maximum volume difference. This indicated that GLORYS12 effectively captured the freshened Pacific Water in these three regions. However, for NCB, there was a lack of correspondence between the core salinity and the peak volume difference. Additionally, the volume of the water masses corresponding to 33–34 in salinity exhibited serrated fluctuations, indicating that the simulation results of GLORYS12

Table 2. Characteristics of the double halocline based on GLORYS12 and *in situ* data

Halocline	Region	2003–2007		2016–2020	
		Volume (GLORYS12) /km³	Thickness (GLORYS12/*in situ*) /m	Volume (GLORYS12) /km³	Thickness (GLORYS12/*in situ*) /m
UH	CAP	25 932	82/87	34 632	110/119
UH	NCB	23 123	79/75	29 845	102/107
UH	NwR	20 521	99/95	28 154	150/129
UH	SCB	31 492	104/98	42 664	141/134
LH	CAP	14 155	45/48	12 643	40/42
LH	NCB	12 585	43/46	13 171	45/47
LH	NwR	11 947	58/53	12 702	61/56
LH	SCB	16 596	55/55	17 026	56/54

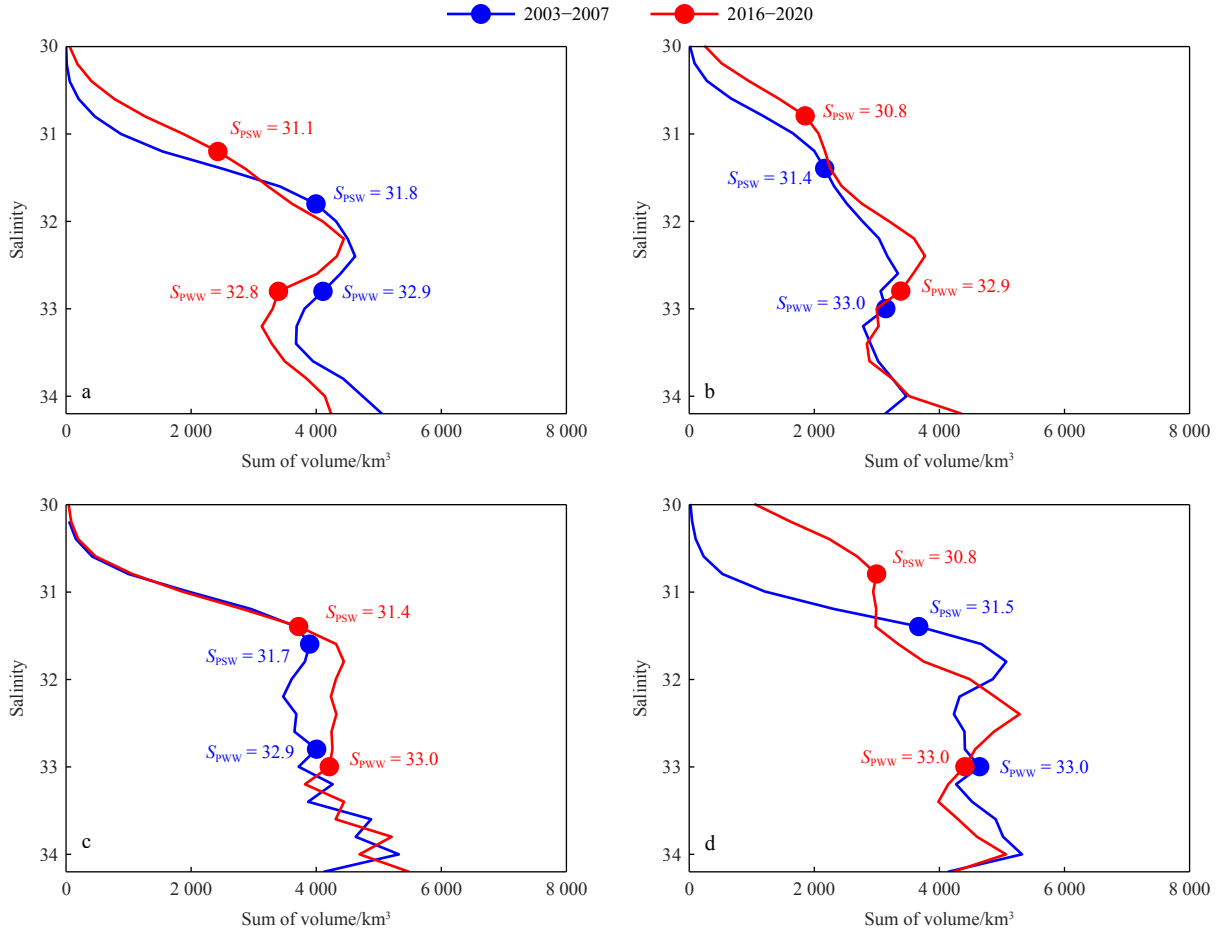


Fig. 8. Salinity versus the sum of volume of the halocline water in CAP (a), NwR (b), NCB (c), and SCB (d) during the periods 2003–2007 and 2016–2020. Salinities marked in blue/red were calculated from *in situ* data.

in NCB were unreliable. Based on the volume difference, we visually identified the core salinity of NPWW for the period 2016–2020 (the green dots in Fig. 9). Finally, the core characteristics of the DH water masses were obtained by integrating both *in situ* data and GLORYS12 and are presented in Table 3.

On average, from the periods 2003–2007 to 2016–2020, the salinity of PSW decreased from 31.6 to 30.9, while the salinity of PWW decreased to 32.4 from 33.0. The intensity of freshening was similar in the Pacific Water, with no significant regional differences (Table 3). Warming of the PSW was more pronounced than the PWW, with the former increasing averagely by 0.4℃ on average. There were minimal changes in the PSW and PWW in the earlier period compared with OPSW and OPWW in the later period, indicating that the Pacific Water before freshening had not completely dissipated and remained at a detectable level. Analysis of the volume differences in water masses in the CAP, NwR, and SCB (Fig. 9) revealed that the increases in NPSW and NPWW significantly exceeded the decreases in OPSW and OPWW. This lag effect led to the coexistence of different Pacific Water masses. Consequently, the average UH thickness increased by (34 ± 12) m in 2022 compared with 2002. Ad-

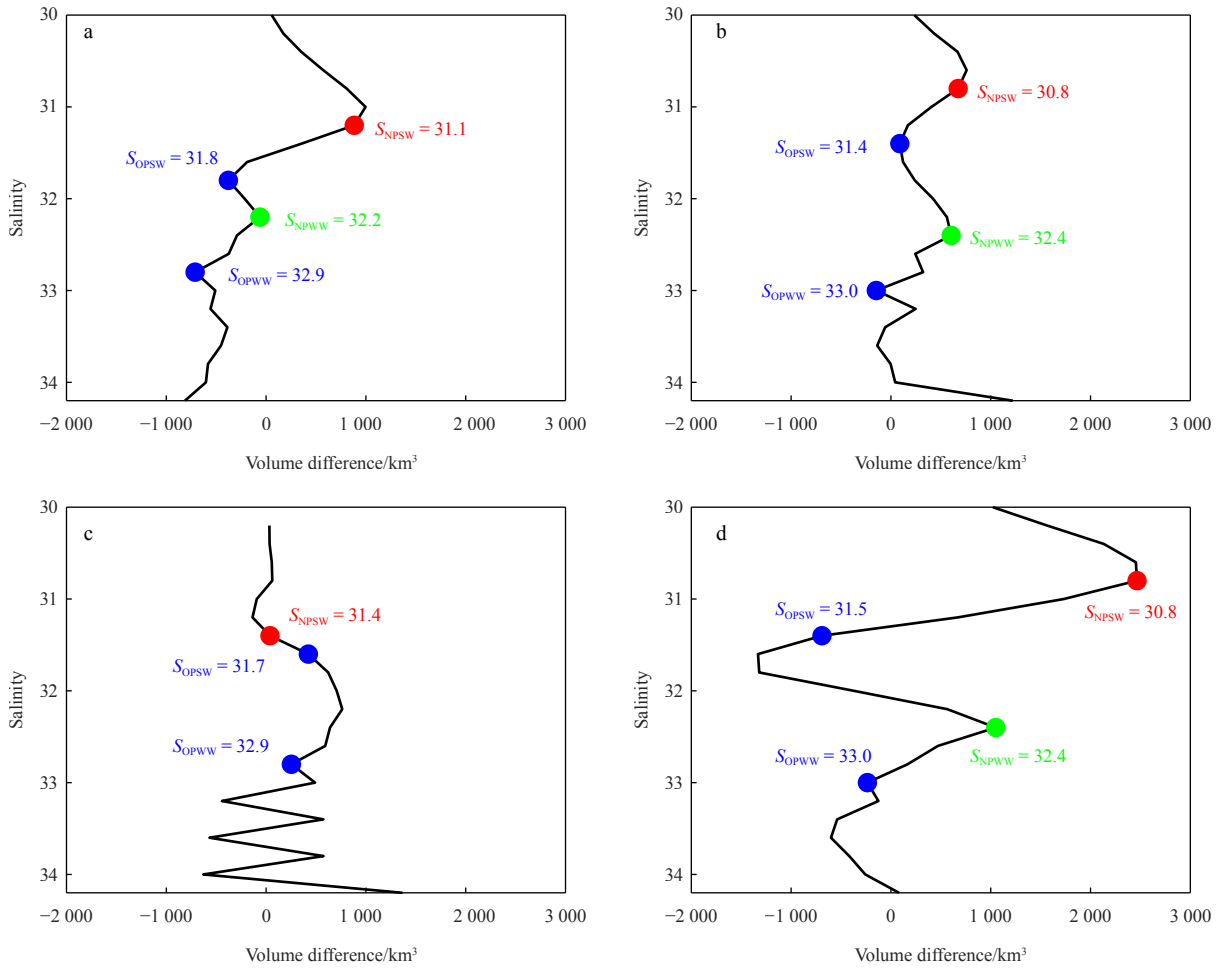


Fig. 9. Salinity versus the difference in the halocline water volume in CAP (a), NwR (b), NCB (c), and SCB (d) during the periods 2016–2020 and 2003–2007. Salinities marked in blue/red were calculated from *in situ* data, while salinities marked in green were identified by visual inspection from GLORYS12.

Table 3. Average temperature and salinity of the core water masses in the DH

Region	2003–2007			2016–2020		
	Water mass	Salinity	Temperature/℃	Water mass	Salinity	Temperature/℃
CAP	–	–	–	NPSW	31.1	−0.39
CAP	PSW	31.8	−0.64	OPSW	31.8	−0.71
CAP	–	–	–	NPWW	32.2	−1.15
CAP	PWW	32.9	−1.54	OPWW	32.9	−1.41
NwR	–	–	–	NPSW	30.8	0.11
NwR	PSW	31.4	−0.21	OPSW	31.4	−0.16
NwR	–	–	–	NPWW	32.4	−1.28
NwR	PWW	33.0	−1.49	OPWW	33.0	−1.31
SCB	–	–	–	NPSW	30.8	0.30
SCB	PSW	31.5	−0.29	OPSW	31.5	−0.29
SCB	–	–	–	NPWW	32.4	−1.28
SCB	PWW	33.0	−1.52	OPWW	33.0	−1.38

Note: − means non-existence.

ditionally, OPWW exhibited varying degrees of loss across the four regions, resulting in a thinning of LH in the later period. In other words, the changes in water masses caused by the positive buoyancy forcing of Pacific Water significantly altered the thickness of the DH.

Furthermore, the LH depth has responded to the interannual pattern of the positive buoyancy forcing. There was a 1-a lag relationship of LH depth between NwR and SCB (Fig. 6), with a correlation of 0.85. Lin et al. (2023b) noted that a branch of the Chukchi Shelf Current flowing into the NwR may eventually shift eastward into SCB, thus becoming part of the Beaufort Gyre. The distance be-

tween the centers of NwR and SCB is approximately 300 km. We chose a typical geostrophic current speed of 1.5 cm/s that allowed us to estimate the time required for the water mass to travel between the two locations as 310 d. Therefore, the lateral transport of the newly ventilated Pacific Water affected the spatial variation of LH depth.

In summary, the DH structure underwent continuous changes from 2002 to 2022; these changes were influenced by the synergistic effects of Ekman pumping, mesoscale eddies, and positive buoyancy forcing of Pacific Water. The first two factors collaboratively regulated the strength of downwelling within the Beaufort Gyre, resulting in spatial variation in halocline depth across the different regions. The positive buoyancy forcing promoted the coexistence of multiple Pacific Water masses that further altered the thickness and depth of the DH.

3.4 *Influence of changes in the DH on the upper ocean*

The stratification of the DH decreased by 14% from 2002 to 2022, with different trends in different periods. Between 2002 and 2012, the notable freshening of Pacific Water led to a significant thickening of the central UH part with low N^2 values (Fig. 7e), consequently causing a decrease in the mean buoyancy frequency (Fig. 10e). The freshening process decelerated from 2012 to 2022, leading to stabilization of the UH thickness and a continued decline in mean buoyancy frequency. Nguyen et al. (2012) noted that the ventilation time of the halocline water in the western Arctic Ocean was 10–21 a. However, our findings indicate that PWW before freshening remained detectable in the DH, with no significant reduction in water volume. This suggests that the LH is difficult to ventilating.

Warming of the Pacific Water has increased the heat content of the DH, from $(3.3 \pm 0.2) \times 10^8$ J/m^2 in 2002 to $(5.4 \pm 1.4) \times 10^8$ J/m^2 in 2022, a 65% increase. The additional heat will melt 0.9 m of sea ice, taking the latent heat of melting to be 2.67×10^5 J/kg and the density of sea ice to be 900 kg/m^3. The average temperature of the OPWW core has increased by 0.15℃ (Table 3), potentially as a result of the mixing of the OPWW with adjacent water masses. In this context, the temperature difference of the LH continued to increase, and the vertical heat flux through the DH exhibited an upward trend, rising from (0.17 ± 0.02) W/m^2 in 2002 to (0.21 ± 0.01) W/m^2 in 2022.

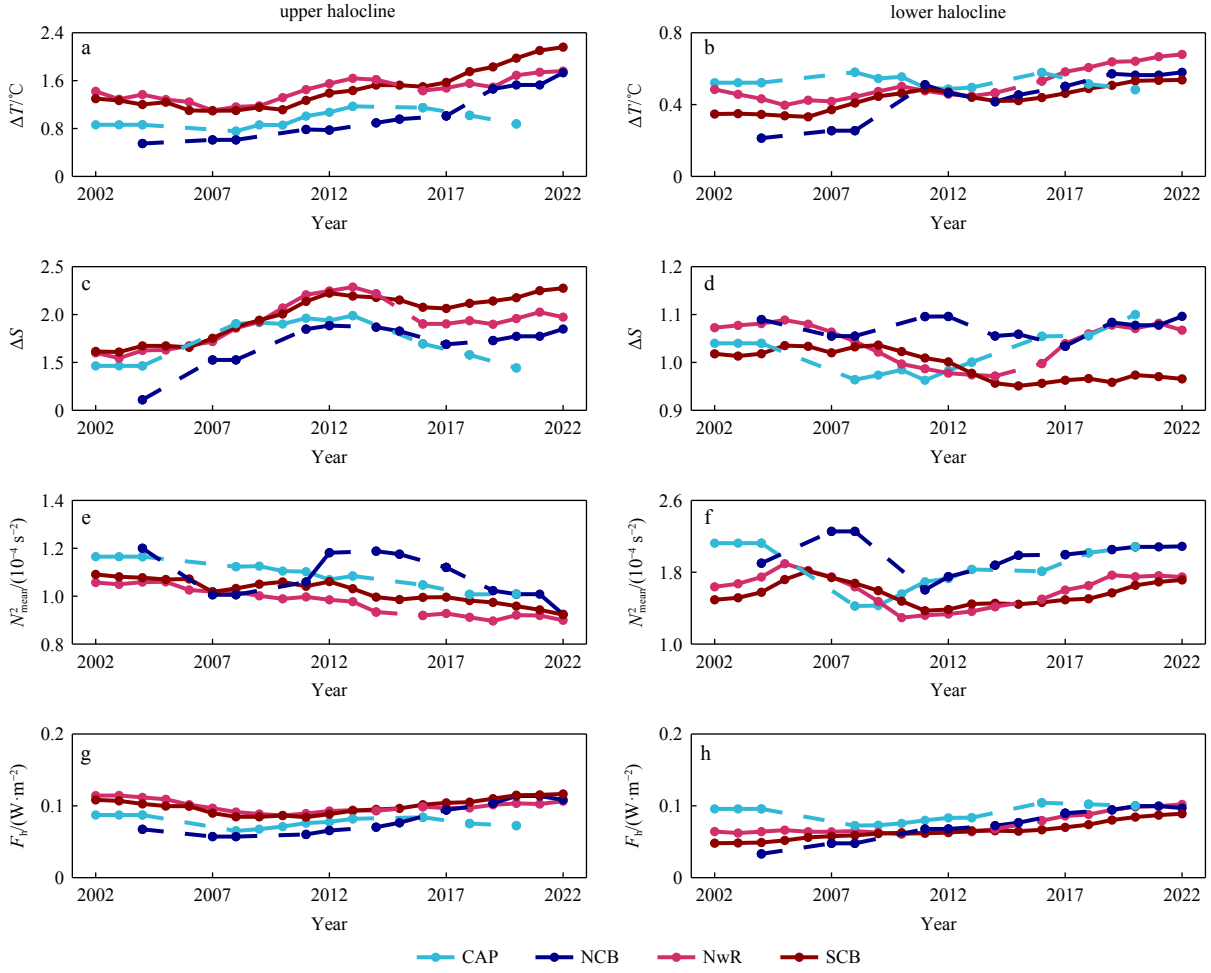


Fig. 10. Time series of regional averages of the temperature (a and b), salinity difference (c and d), mean buoyancy frequency (e and f), and vertical heat flux (g and h) of the upper halocline and lower halocline during the period 2002–2022.

4 Conclusions

This study has presented a comprehensive analysis of the spatial variation and interannual differences in the DH in the western Arctic Ocean, using *in situ* measurements and the reanalysis data. We investigated the mechanisms contributing to the changes in depth and thickness of the DH, ultimately offering a quantitative assessment of halocline stratification. The main conclusions are as follows.

(1) The upper western Arctic Ocean is characterized by a DH that contrasts sharply with the single halocline in the eastern Arctic Ocean. The DH is particularly prominent in the Northwind Ridge and the southern Canada Basin. In comparison to the upper halocline, the lower halocline exhibits a pronounced vertical density gradient and stronger stratification.

(2) Between 2002 and 2022, the DH increased in thickness by (31 ± 14) m, with the freshwater and heat contents increasing by 42% and 65%, respectively. Overall, the stratification of the DH has gradually decreased, resulting in an increase in vertical heat flux through the DH that rose from (0.17 ± 0.02) W/m^2 in 2002 to (0.21 ± 0.01) W/m^2 in 2022.

(3) The depth and thickness of the halocline are influenced by two primary mechanisms: the balance between Ekman pumping and mesoscale eddies, and the positive buoyancy forcing from the Pacific Water. The former mechanism is closely associated with the interannual variability of the halocline depth. Ekman pumping regulates the upper boundary depth of the UH and the depression of the LH across the four regions. The positive buoyancy forcing from the Pacific Water alters the thickness and stratification of the DH. The buoyancy gain leads to a shoaling of New Pacific Water, causing the sinking of the old Pacific Water. Meanwhile, the volume of OPWW has remained relatively stable, and its core thermohaline characteristics have not undergone significant changes, suggesting that the ventilation of the halocline has been significantly inhibited.

The DH in the western Arctic Ocean thickened, warmed, and became less stratified between 2002 and 2022, indicating that the heat content is continuously increasing and is likely to reach the seasonal halocline and mixed layer. The increased heat content will likely accelerate the retreat of sea ice.

References

Aagaard K, Coachman L K, Carmack E. 1981. On the halocline of the Arctic Ocean. Deep Sea Research Part A. Oceanographic Research Papers, 28(6): 529–545

Armitage T W K, Manucharyan G E, Petty A A, et al. 2020. Enhanced eddy activity in the Beaufort Gyre in response to sea ice loss. Nature Communications, 11(1): 761, doi: 10.1038/s41467-020-14449-z

Bertosio C, Provost C, Athanase M, et al. 2022. Changes in Arctic halocline waters along the East Siberian slope and in the Makarov Basin from 2007 to 2020. Journal of Geophysical Research: Oceans, 127(9): e2021JC018082, doi: 10.1029/2021JC018082

Bourgain P, Gascard J C. 2011. The Arctic Ocean halocline and its interannual variability from 1997 to 2008. Deep-Sea Research Part Ⅰ: Oceanographic Research Papers, 58(7): 745–756, doi: 10.1016/j.dsr.2011.05.001

Chan P, Halfar J, Williams B, et al. 2011. Freshening of the Alaska Coastal Current recorded by coralline algal Ba/Ca ratios. Journal of Geophysical Research: Biogeosciences, 116(G1): G01032

Darby D A, Bischof J F. 2004. A Holocene record of changing Arctic Ocean ice drift analogous to the effects of the Arctic Oscillation. Paleoceanography, 19(1): PA1027

Hibler III W D. 1979. A dynamic thermodynamic sea ice model. Journal of Physical Oceanography, 9(4): 815–846, doi: 10.1175/1520-0485(1979)009<0815:ADTSIM>2.0.CO;2

Hibler III W D, Bryan K. 1987. A diagnostic ice–ocean model. Journal of Physical Oceanography, 17(7): 987–1015, doi: 10.1175/1520-0485(1987)017<0987:ADIM>2.0.CO;2

Kenigson J S, Gelderloos R, Manucharyan G E. 2021. Vertical structure of the Beaufort Gyre halocline and the crucial role of the depth-dependent eddy diffusivity. Journal of Physical Oceanography, 51(3): 845–860, doi: 10.1175/JPO-D-20-0077.1

Korhonen M, Rudels B, Marnela M, et al. 2013. Time and space variability of freshwater content, heat content and seasonal ice melt in the Arctic Ocean from 1991 to 2011. Ocean Science, 9(6): 1015–1055, doi: 10.5194/os-9-1015-2013

Lin Peigen, Pickart R S, Heorton H, et al. 2023a. Recent state transition of the Arctic Ocean's Beaufort Gyre. Nature Geoscience, 16(6): 485–491, doi: 10.1038/s41561-023-01184-5

Lin Peigen, Pickart R S, Weingartner T J, et al. 2023b. Formation and circulation of newly ventilated winter water in the western Beaufort Sea. Progress in Oceanography, 216: 103068, doi: 10.1016/j.pocean.2023.103068

Lique C, Guthrie J D, Steele M, et al. 2014. Diffusive vertical heat flux in the Canada Basin of the Arctic Ocean inferred from moored instruments. Journal of Geophysical Research: Oceans, 119(1): 496–508, doi: 10.1002/2013JC009346

Liu Zhongfang. 2022. Arctic sea ice decline and its driving mechanisms. Chinese Journal of Nature (in Chinese), 44(1): 39–46

McPhee M G, Proshutinsky A, Morison J H, et al. 2009. Rapid change in freshwater content of the Arctic Ocean. Geophysical Research Letters, 36(10): L10602

Meneghello G, Marshall J, Cole S T, et al. 2017. Observational inferences of lateral eddy diffusivity in the halocline of the Beaufort Gyre. Geophysical Research Letters, 44(24): 12331–312338

Nguyen A T, Kwok R, Menemenlis D. 2012. Source and pathway of the western Arctic upper halocline in a data-constrained coupled ocean and sea ice model. Journal of

Physical Oceanography, 42(5): 802–823, doi: 10.1175/JPO-D-11-040.1

Polyakov I V, Pnyushkov A V, Carmack E C. 2018. Stability of the Arctic halocline: A new indicator of Arctic climate change. Environmental Research Letters, 13(12): 125008, doi: 10.1088/1748-9326/aaec1e

Polyakov I V, Rippeth T P, Fer I, et al. 2020. Weakening of cold halocline layer exposes sea ice to oceanic heat in the eastern Arctic Ocean. Journal of Climate, 33(18): 8107–8123, doi: 10.1175/JCLI-D-19-0976.1

Polyakov I V, Timokhov L A, Alexeev V A, et al. 2010. Arctic ocean warming contributes to reduced polar ice cap. Journal of Physical Oceanography, 40(12): 2743–2756, doi: 10.1175/2010JPO4339.1

Rudels B, Anderson L G, Jones E P. 1996. Formation and evolution of the surface mixed layer and halocline of the Arctic Ocean. Journal of Geophysical Research: Oceans, 101(C4): 8807–8821, doi: 10.1029/96JC00143

Shi Jiuxin, Zhao Jinping, Li Shujiang, et al. 2005. A double-Halocline structure in the Canada basin of the Arctic Ocean. Acta Oceanologica Sinica, 24(6): 25–35

Shimada K, Itoh M, Nishino S, et al. 2005. Halocline structure in the Canada Basin of the Arctic Ocean. Geophysical Research Letters, 32(3): L03605

Shimada K, Kamoshida T, Itoh M, et al. 2006. Pacific Ocean inflow: influence on catastrophic reduction of sea ice cover in the Arctic Ocean. Geophysical Research Letters, 33(8): L08605

Shu Qi, Wang Qiang, Årthun M, et al. 2022. Arctic Ocean Amplification in a warming climate in CMIP6 Models. Science Advances, 8(30): eabn9755, doi: 10.1126/sciadv.abn9755

Steele M, Morison J, Ermold W, et al. 2004. Circulation of summer Pacific halocline water in the Arctic Ocean. Journal of Geophysical Research: Oceans, 109(C2): C02027

Timmermans M L, Marshall J. 2020. Understanding Arctic Ocean circulation: A review of ocean dynamics in a changing climate. Journal of Geophysical Research: Oceans, 125(4): e2018JC014378, doi: 10.1029/2018JC014378

Timmermans M L, Marshall J, Proshutinsky A, et al. 2017. Seasonally derived components of the Canada Basin halocline. Geophysical Research Letters, 44(10): 5008–5015, doi: 10.1002/2017GL073042

Timmermans M L, Proshutinsky A, Golubeva E, et al. 2014. Mechanisms of Pacific summer water variability in the Arctic's Central Canada Basin. Journal of Geophysical Research: Oceans, 119(11): 7523–7548, doi: 10.1002/2014JC010273

Timmermans M L, Toole J, Krishfield R. 2018. Warming of the interior Arctic Ocean linked to sea ice losses at the basin margins. Science Advances, 4(8): eaat6773, doi: 10.1126/sciadv.aat6773

Toole J M, Timmermans M L, Perovich D K, et al. 2010. Influences of the ocean surface mixed layer and thermohaline stratification on Arctic Sea Ice in the Central Canada Basin. Journal of Geophysical Research: Oceans, 115(C10): C10018

Weingartner T J, Cavalieri D J, Aagaard K, et al. 1998. Circulation, dense water formation, and outflow on the Northeast Chukchi Shelf. Journal of Geophysical Research: Oceans, 103(C4): 7647–7661, doi: 10.1029/98JC00374

Woodgate R A, Peralta-Ferriz C. 2021. Warming and freshening of the Pacific Inflow to the Arctic from 1990–2019 implying dramatic shoaling in Pacific winter water ventilation of the Arctic Water Column. Geophysical Research Letters, 48(9): e2021GL092528, doi: 10.1029/2021GL092528

Woodgate R A, Weingartner T, Lindsay R. 2010. The 2007 Bering Strait oceanic heat flux and anomalous Arctic sea-ice retreat. Geophysical Research Letters, 37(1): L01602

Ye Kunhui, Woollings T, Sparrow S N, et al. 2024. Response of winter climate and extreme weather to projected Arctic sea-ice loss in very large-ensemble climate model simulations. npj Climate and Atmospheric Science, 7(1): 20, doi: 10.1038/s41612-023-00562-5

Zhang Jinlun, Rothrock D A, Steele M. 1998. Warming of the Arctic Ocean by a strengthened Atlantic inflow: Model results. Geophysical Research Letters, 25(10): 1745–1748, doi: 10.1029/98GL01299

Zhao Jinping, Shi Jiuxin, Wang Zhaomin, et al. 2015. Arctic amplification produced by sea ice retreat and its global climate effects. Advances in Earth Science (in Chinese), 30(9): 985–995

Zhong Wenli, Steele M, Zhang Jinlun, et al. 2018. Greater role of geostrophic currents in Ekman dynamics in the western Arctic Ocean as a mechanism for Beaufort Gyre stabilization. Journal of Geophysical Research: Oceans, 123(1): 149–165, doi: 10.1002/2017JC013282

Zhong Wenli, Steele M, Zhang Jinlun, et al. 2019a. Circulation of Pacific Winter Water in the western Arctic Ocean. Journal of Geophysical Research: Oceans, 124(2): 863–881, doi: 10.1029/2018JC014604

Zhong Wenli, Zhang Jinlun, Steele M, et al. 2019b. Episodic extrema of surface stress energy input to the western Arctic Ocean contributed to step changes of freshwater content in the Beaufort Gyre. Geophysical Research Letters, 46(21): 12173–12182, doi: 10.1029/2019GL084652